The Viscosity of Water at High Pressures and High Temperatures: A Random Walk through a Subduction Zone

Thesis

Presented in Partial Fulfillment of the Requirements for the Degree Master of Science in the Graduate School of The Ohio State University

By

Jeff S. Pigott, B.A.

Graduate Program in Earth Sciences

The Ohio State University

2011

Thesis Committee:

Wendy R. Panero, Advisor

Michael Barton

David Cole

Abstract

The viscosity of water is a first-order constraint on the transport of material from a subducting plate to the mantle wedge. The viscosity of fluids that are released during the dehydration of hydrous minerals during subduction can vary by more than 9 orders of magnitude between the limits of pure liquid water and silicate melts. Accurate determination of low viscosities (<1 mPa·s) for liquids at simultaneous high pressures (>1 GPa) and high temperatures (>373 K) is hindered by the geometry and sample size of high-pressure devices. Here the viscosity of water at pressures representative of the deep crust and upper mantle through use of Brownian motion in the hydrothermal diamond anvil cell (HDAC) is reported. By tracking the Brownian motion of 2.8 and 3.1 micron polystyrene spheres suspended in H_2O, the viscosity of the water at high pressure and high temperature can be determined *in situ* using Einstein's relation. Accuracies of 3-10% are achieved and measurements are extended to pressures relevant to fluid release from subducting slabs and temperatures up to 150% of the melting temperature. Unhampered by wall effects of previous methods, the results from this study are consistent with a homologous temperature dependence of water viscosity in which the viscosity is a function of the ratio of the temperature to the melting temperature at a given pressure. Based on the homologous temperature dependence of water, transport times for fluids released from subducted plates inferred from geochemical proxies are too short for

transport via porous flow alone, and suggest transport through a combination of channel-flow and porous flow implying hydrofracturing at 50-150 km depth.

Dedication

Dedicated to Carmen LeEtta Pigott

Acknowledgments

I would like to sincerely thank my advisor, Dr. Wendy Panero, who has advised me during my time as a graduate student working in mineral physics. She has dedicated herself to teaching me how to be a successful student and has worked to ensure that I will develop into a productive member of the high-pressure research community. Furthermore, I would like to thank my committee members, Michael Barton and David Cole, along with Yo Chin, for their helpful discussions and feedback as this project progressed.

I wish to extend thanks to Daniel Reaman for his assistance with the technical aspects of my experiments. The time that he spent teaching me the nuances of diamond anvil cell research was significant in the successful completion of this project.

I want to recognize the AAPG Grants-in-Aid program for the funding used to conduct this research. Additionally, I would like to thank Jason Kabbes, Sara Whitaker, Tim Leftwich, Kaitlin Walsh, William Bassett and the University of Michigan for their contributions to this work.

I would also like to acknowledge CIDER (Grant- EAR/CSEDI: #0434151 and #0968979), COMPRES, and OSU for the funding to present this work at professional meetings giving me the chance to engage in helpful discussions.

Finally, I would like to profess a genuine thank you to my wonderful fiancée, Mary Dougherty, as well as my friends and family for the time and interest that they invested in me as I dedicated myself to academics.

Vita

June 21st, 1979……………………………………………..…...Born – Youngstown, Ohio

June 1997..Graduated – East Liverpool
High School, East Liverpool, Ohio

March 2002...B.A. Sociology, The Ohio State
University, Columbus, Ohio

January 2009 – present………………………………...Graduate Teaching Associate, The
Ohio State University

Publications

Goldsmith, S.T., A.E. Carey, B.M. Johnson, S.A. Welch, W.B. Lyons, W.H. McDowell, J.S. Pigott **(**2010), Stream geochemistry, chemical weathering and CO_2 consumption potential of andesitic terrains, Dominica, Lesser Antilles. *Geochemica et Cosmochemica Acta, 74*, 85-103.

Fields of Study

Major Field: Earth Sciences

Table of Contents

List of Tables

List of Figures

Chapter 1

Introduction

Water in subduction zone processes plays a key role in mantle geochemistry and geodynamics. Arc volcanism is attributed to ‘flux melting’ of the mantle wedge caused by release of H_2O during dehydration reactions involving hydrous minerals at ~100 km depth (Fig. 1) [*Schmidt and Poli,* 1998]. The water released from dehydration reactions saturates the surrounding material, lowering the solidus temperature and melting point. The influx of water shifts the solidus of mantle wedge minerals to initiate buoyant partial melting, and therefore the formation of the overlying volcanic arc [*Van Keken,* 2003]. The spatial relationship between the volcanic arc and pressure-temperature stability fields of constituent hydrous phases can be coupled with isotopic signatures of arc-volcanic rocks in order to constrain the temporal relationship between slab dehydration and melt transport [*Turner et al.,* 2001*; Sigmarrsson et al.,* 2002*; Van Keken,* 2003]. The majority of water released into the overlying mantle wedge is a result of several reactions over a range of pressures, temperatures, and water fugacities. The breakdown of the hydrous minerals, chlorite and serpentine, occurs at ~105 km [*Iwamori,* 1998]. Large columns of the mantle are immediately hydrated because asthenospheric mantle peridotite can only dissolve a few hundred parts per million water, and is associated with decrease in viscosity of up to a factor of 100 [*Arcay et al.*, 2005].

Dehydration of subducted slabs has been associated with deep-focus seismic activity to depths of 300 km due to brittle deformation of the slab during dehydration reactions [*Meade and Jeanloz,* 1991; *Raleigh and Paterson,* 1965]. In addition, fluid flowing through propagating dykes might serve to explain earthquakes in the deep upper mantle and transition zone [*Richard et al*., 2007]. Even though the location of seismic events appears to be directly related to the depth range in which hydrous minerals lose most of their crystallographically bound H_2O, the mode and direction of fluid flow remains unanswered [*Hacker*, 2003].

The mechanics of water transport from the subducted slab to the mantle wedge are not entirely understood, as there are a number of possible mechanisms. Hydrofracturing may cause conduits to open and allow for the free flow of water. Based on elastic fracture mechanics coupled with geological observations, *Davies* [1999] found that cracks ~1 - 20 cm wide and ~0.6 - 3 km in length may form perpendicular to the surface of a subducting plate at depths relevant to the dehydration of oceanic crust, 90 – 160 km. Channels may also be generated in the form of normal faults due to bending of the slab and subsequent negative pressure gradients allowing flow of fluids into the deep slab [*Faccenda*, 2009]. Petrologic constraints also show that the initial stages of fluid transport through the mantle directly above the slab is dominated by microcracks developed by hydrofracturing during the breakdown of serpentine [*Padron-Navarta et al.,* 2010].

A second possibility is the porous flow of aqueous fluids along grain boundaries at pressures >1 GPa if there is a decrease in the dihedral angles to <60° (the critical value for interconnected flow) due to an increase in silicate solubility in water with increasing pressure. This reduction in the dihedral angle in the olivine-H_2O system prevents formation of isolated pockets of fluid [*Iwamori,* 1998; *Mibe et al.,* 1999]. However, fluid may exist in isolated interstitial pockets in eclogite between depths of 90 and 150 km preventing vertical flow of buoyant fluid via this process [*Mibe et. al.,* 2003].

Finally, chemical diffusion of hydroxyl ions through the crystal lattices of mantle silicates [*Demouchy and Mackwell,* 2003] may play a role in fluid transport under certain conditions. In this case, water transport is through the solid crystal or along grain boundaries as OH. This is a very slow material transport mechanism and flow is limited to sub-kilometer-scale distances.

Geochemical evidence suggests that it may take as little as 1000-8000 years for aqueous fluid migration from the point of release from a subducting slab to eruption in arc volcanism in some subduction zones [*Turner et al.,* 2001; *Sigmarrsson et al.,* 2002]. These timescales suggest a transport mechanism of either hydrofracturing or porous flow. Porous flow is really grain boundary transport due to the extremely low porosity likely found in the mantle. Assuming each possible mechanism acts independently, predicted time scales differ by more than an order of magnitude from the geochemical observations and from each other assuming pure water and low-pressure constraints. Thus, the viscosity of the fluid is a first-order constraint on the transport mechanism of material from the subducted plate to the overlying mantle wedge.

The pressure and temperature dependence of water viscosity and the effect of water on mantle viscosity are therefore crucial to understanding the rheological, mechanical, and thermal regimes of the upper mantle. An experimentally derived model of water viscosity in subduction zones is necessary to integrate geochemical and geodynamical models for fluid transport and melt migration mechanisms and timescales relevant to arc volcanism.

The diamond anvil cell (DAC) can be used as a viscometer for fluids under extreme conditions [*King et al.*, 1992]. Viscosity measurements have been made in the DAC on a variety of fluids including oxygen, nitrogen, carbon dioxide [*Abramson*, 2005, 2008, 2009], methanol, 4:1 methanol-ethanol [*Grocholski and Jeanloz*, 2005], water [*Abramson*, 2007], along with solutions comprised of solvents such as tetrahydrofuran, chloroform, NaCl-water [*Cook et al.*, 1992].

Existing DAC viscometers have been limited in their ability to measure viscosities of fluids at simultaneous high pressures and high temperatures. All of the viscosity measurements on fluids compressed in a DAC used a rolling or falling sphere approach [*King et al.*, 1992] where 10-60 μm spheres roll or slide along one of the diamond faces of a tilted diamond cell. The terminal velocities of falling spheres are calculated by recording the motion of the sphere and viscosities are determined using modified Stoke's Law equations. A wall correction is required because the falling sphere is affected by viscous drag from both the gasketed sample chamber and the diamond faces. Accurate calculation of the wall correction coefficient poses a problem. The calculation of the wall correction may not remain constant if the sphere does not have the same starting point and trajectory after tilting in different experimental runs [*King et al.*, 1992]. The wall correction is empirical and is a strong function of the radius of the sphere, width of the channel, and frictional drag coefficients [*Schiller*, 1931; *Schiller*, 1932]. The commonly used Faxen correction function has been shown to over-estimate the viscosity of silicate melts [*Kahle*, 2003]. Also, a major problem with the falling and rolling sphere experiment is adhesiveness of the spheres to chamber walls.

Published experimental water viscosity data at high pressure (>1 GPa) and high temperature (>373 K) derived by such methods are sparse at the conditions relevant to subduction zones (Fig. 2). The viscosity of water has been experimentally determined up to 6 GPa at 573 K using a rolling ball technique in the diamond cell. These experiments measured viscosities between 0.3 and 3.3 mPa·s [*Abramson*, 2007], or 30% to 330% of the ambient water viscosity. In analogous experiments, the measured viscosities range from 0.1 mPa-s (N_2 at 0.3 GPa and 294 K) to 4.7 mPa-s (CO_2 at 8 GPa and 673 K), reflecting little more than an order of magnitude variation over ~400 K. The lower limit of ~0.1 mPa-s is possibly a combination of (1) difficulty in determining terminal velocity in a Stokes' flow regime and (2) lack of calibration for the effects of gasket thinning (and therefore greater wall effects) at high pressures.

The problems with the rolling or sliding sphere approach can be circumvented by using the theory of Brownian motion coupled with the hydrothermal diamond anvil cell. In this approach, the size of the particles is significantly smaller than used for a sliding sphere, and therefore subject to smaller wall effects.

Brownian motion is the random movement of microscopic particles suspended in a stationary liquid. The movement is due to molecular motions according to molecular-kinetic theory of heat [*Einstein,* 1926]. The mean square displacement (MSD) of a particle observed in two dimensions as a function of time is:

$$< [r(t)]^2 >= \frac{4k_b T}{6\pi\eta a} t \qquad \textbf{(1)}$$

where, k_b is Boltzmann's constant, T is temperature in Kelvin, a is the radius of the particle, η is the viscosity of the fluid, and t is time. The viscosity of the fluid is therefore calculated from the mean-square displacement of the particle as a function of time. Brownian motion is observed through the optically transparent diamonds contained in both the DAC and the HDAC, then used to measure the viscosity of the fluid. Brownian motion has been used to verify Einstein's derivation of the relationship between the diffusion coefficient and the viscosity of molecules dissolved in a liquid along with confirming Perrin's calculations of Avogadro's number [*Newburgh et. al.,* 2006].

The objective of this study is to conduct experiments using the HDAC coupled with Brownian motion to measure the viscosity of pure water at simultaneous high-pressures and high-temperatures. The experimentally derived viscosity values can be used to predict the timescales of fluid transport in the mantle wedge. Comparison of predicted timescales with geochemical observations can elucidate the material transport mechanics in subduction zones.

Chapter 2

Methods

Both a DAC and a HDAC (Fig. 3) [*Bassett et al.,* 1993; *Wilke et al.,* 2010]] are used for viscosity experiments. The DACs contain two opposing diamonds with inner culet diameters of 350 μm or 500 μm. The WC seats in the HDAC are wrapped with chromel heating wires then connected to a 100-240 V power supply. The sample is heated from both the top and bottom by conduction of heat through the WC seats and diamonds which allows for even heating of the sample [*Bassett et al.,* 1993]. The sample temperature is measured using K-type chromel-alumel thermocouples with a diameter of 0.13 mm. The thermocouples are wrapped around both diamonds. The power supplied to the top and bottom heaters are controlled separately and the temperatures are controlled to within 5 K of each other. Due to the extremely high thermal conductivity of diamond and the fact that the temperatures are essentially the same, the sample is assumed to be at the temperature measured by the thermocouples with a negligible temperature gradient.

2.75(7) or 3.1(2) µm polystyrene microspheres with a density of 1 g/cm^3 and a small Cr-doped ruby chip for pressure measurement are added to pure water and loaded into a diamond anvil cell (Fig. 4). These spheres were chosen because they have a density that is equal to water and are therefore neutrally buoyant. Gaskets (stainless steel or rhenium) are pre-indented to thicknesses of 140-190 µm, controlling the separation of the diamonds. Effort is made to keep the gaskets as thick as possible to minimize wall drag effects caused by the diamond surfaces, while simultaneously carefully measuring the thickness after the experiment for monitoring and calibration. A 260 µm diameter hole is drilled in the center of the pre-indention.

The samples are compressed to pressure then resistively heated. Pressures are determined based on *in situ* observation of the H_2O liquid-solid phase transition upon heating and cooling coupled with room-temperature ruby fluorescence measurements before and after the experiments [*Chijoke et al.*, 2005]. The sample is compressed at room temperature to >1 GPa and the formation of solid H_2O is verified by the lack of Brownian motion and the appearance of visible crystals. The temperature is increased to the melting point and the total pressure of the sample at the solid-liquid phase boundary is calculated based on the melting curves (Fig. 5) of Ice VI [*Choukran et al*,. 2007] and Ice VII [*Lin et al.*, 2004]. The liquid-solid phase change upon cooling is observed (Fig. 6) as an additional pressure measurement. Thus, there are three or four constraints on the pressure of the sample in these experiments, depending on where the post-heating pressure is located in the H_2O phase diagram.

While monitoring the gasket for shape changes upon heating, the sample is assumed to be a constant volume and the contribution to the total pressure of the sample from thermal pressure is calculated from the thermodynamic relationship [*Poirer*, 2000]:

$$\left(\frac{\partial P}{\partial T}\right)_V = \alpha K_T \qquad \textbf{(2)}$$

where P is pressure, V is volume, α is the coefficient of volumetric thermal expansion and K_T is the isothermal bulk modulus at 300 K. By rewriting equation (**2)**, the total pressure of the sample is approximated as:

$$P_{tot} = P_{ref} + \alpha K_T \Delta T \qquad \textbf{(3)}$$

where P_{tot} is the total pressure and P_{ref} is a reference pressure (Table 1). P_{ref} is the pressure of crystallization when observed upon cooling, as this is the best approximation of the pressure of the liquid sample allowing for high P-T relaxation of the sample assembly. If no crystallization occurs upon cooling, then pressure from the ruby fluorescence after heating is used. The melting pressure is avoided as the P_{ref} because of likely volume relaxation during the solid-liquid phase transition. Values of α and K_T are assumed to be 2.76 x 10^4 K^{-1} and 2.22 GPa, respectively [*Kell*, 1975].

A Nikon CoolPix™ digital camera connected to the ocular of the microscope records the particle motion in the HDAC with a total magnification from the microscope and camera of ~300-600X. Brownian motion of the polystyrene spheres is digitally recorded for 40 seconds at a rate of 15 frames/second and a resolution of 1-2 pixels/micron. The video is then analyzed using a particle tracking velocimetry (PTV) program written in MATLAB [*Grant*, 1997]. While the water is in the liquid phase, Brownian motion of the polystyrene microspheres is observed during all of the experimental runs. The random movement of the spheres is observed visually by looking through the microscope and subsequently verified by particle tracking analysis. If there is not preferential displacement of all of the particles in the same direction over the time scales of the experiment, the random walk of a particle's trajectory (Fig. 7) confirms that the only forces acting on the particle is the force of the surrounding water. If a particle appears to be moving due to forces other than those of the surrounding fluid then the particle is not used in the viscosity calculations. Forces acting on the particles other than the molecular forces of the water can be caused by pressure gradients, particle-particle interaction, or interaction with the sample chamber wall. If the particle adheres to one of the diamond faces, the Brownian motion ceases. However, these particles generally are out of focus and therefore are not analyzed.

The PTV program tracks the position of the particle at every frame by maximizing the cross-correlation of color values between frames and assigns a distance value proportional to the pixel dimension (*dpix*) which varies with differing camera magnification between experiments. The pixel dimensions in microns are calibrated using meshes with 120 and 150 wires/inch.

Einstein [1926] showed that the mean displacement in the *x*-direction of a particle suspended in a fluid is related to the diffusion coefficient by:

$$r_x = \sqrt{2Dt} \tag{4}$$

where *D* is the diffusion coefficient. At ambient conditions, a particle is displaced a distance on the order of the particle's diameter during a time of 1 s, assuming a fluid with a viscosity such as that of water. This prediction is consistent with the room temperature observations in this study. Equation **(4)** is rewritten to include the displacement in 2 dimensions such that:

$$r_{xy} = \sqrt{4Dt} \tag{5}$$

Equation **(5)** is rewritten in the form of equation **(1)** and holds true as long as the time steps are greater than 10^{-7} s and the size of the spherical solute is much greater than the size of the solvent molecules: the experiments conducted in this study conform to these criteria. The path length *r*, on average, is the same for both dimensions and for all particles in suspension therefore, a weighted average of the single particle slopes is used to calculate the viscosity of water. Equation (**5**) is based on a two dimensional projection of a three dimensional process thus the three dimensional effects in our experiments are justifiably neglected.

By summing the squares of the vector distances at each time step, the MSD is calculated by:

$$<[r(t)]^2>=\{[(x(t+\tau)-x(t)]^2+[y(t+\tau)-y(t)]^2\} \tag{6}$$

where x and y are the vector positions projected in 2 dimensions and τ is the time interval between frames. The viscosity is calculated from equation **(1)** with the slope of the line $<r^2>$ as a function of t. Multiple particles are tracked during each analysis and the fluid viscosity is calculated using the weighted mean of single particle slopes.

Brownian motion of colloidal spheres is influenced by hydrodynamic drag caused by parallel and cylindrical walls [*Dufresne et al*. 1997; *Mukai et al.,* 2006]. DAC experiments are conducted at 291 K and 0.1 MPa to calibrate the effects of wall drag due to the diamond surfaces and gasket walls. The apparent viscosity of the water as a function of gasket thickness and gasket hole circumference is used to quantify the wall effects (eqn. 7; Fig. 8). Apparent viscosity asymptotically approaches the infinite-thickness value at ~ 250 μm (Fig. 8). Therefore, all high-pressure, high-temperature experiments are performed with 260 μm gasket holes to avoid wall effects from the gasketting, and correcting based on the calibration as a function of gasket thickness only. The deviation of the apparent viscosity from the true viscosity (Fig. 8) is assumed to have the functional form:

$$\log(\eta_{app}) = \log(\eta_0) + \frac{A}{D} \tag{7}$$

where η_{app} is the apparent viscosity calculated from the measured diffusion coefficient, η_0

is the true viscosity at infinite distance from a wall, *A* is an empirically derived constant, and *D* is the smallest spacing between walls, either the gasket thickness or sample chamber diameter. The errors used in the weighted fit according to equation (**7**) are based on the weighted average of the viscosities calculated from single particles. The fitting parameters using equation **(7)** are η_0 = 1.054 mPa·s (fixed) and *A*=11(2) µm. The fitting parameter η_0 is based on the viscosity at an infinite distance from a wall and is thus fixed to the true water viscosity reported by *Aleksandrov and Trakhtengerts* [1976] and the derived correction is applied to all of the measured apparent viscosities. The *D* value used in the corrections is based on gasket thickness after cooling and decompression. Effort is made to analyze particles >4*a* from neighboring particles (Fig. 9) in order to minimize the influence of interacting spheres [*Crocker*, 1997].

The temperature dependence of fluid viscosity is approximated by an exponential relationship,

$$\eta = \eta_0 e^{-bT} \tag{8}$$

where η is the viscosity, *T* is temperature, η_0 which represents the viscosity at 0 K with units of Pa·s, and *b* is an empirically derived constant that is related to the activation enthalpy. Equation **(8)** is rewritten to include the effects of pressure as:

$$\eta = \eta_0 e^{\frac{-gT}{T_m}} \tag{9}$$

where T_m is the melting temperature and g is an empirically derived constant. The relationship predicts a constant viscosity for a constant ratio of the temperature to the melting temperature, T/T_m. Many material properties dependent on activation processes vary according to the melting temperature when there is no significant structural change in the liquid [*Terasaki et al.*, 2004]. The homologous temperature relationship is based in the assumption that the activation volume and energy scales with the melting temperature in solids and liquid metals [*Poirier*, 1988, 2000].

Chapter 3

Results

The viscosity of pure water was measured to 2.8 GPa and 523 K in an HDAC using the Brownian motion method to constrain the mechanism by which fluid flows through porous media. The determined viscosities overestimate the viscosity by less than 10% at ambient pressure and temperature. The ~10% misfit likely arises from viscous drag caused by a many-particle system or an underestimate of the combined drag effects of the diamond faces coupled with the effects of the sample chamber wall, and represents a remaining inherent uncertainty in the measurements based on this method.

At 2.8 GPa and 523 K the apparent viscosity varies between 0.2-0.41 mPa·s for different particles (Fig. 10). A weighted average of the single particle, mean-squared displacements yield a viscosity of 0.32(8) mPa·s.

Viscosity is a secondary thermodynamic property and therefore varies with pressure and temperature. After correcting for the effects of wall drag, the results show values for viscosity that range from 2(2) mPa·s at 292 K and 590 MPa to 0.13(5) mPa·s at 473 K and 1.57 GPa (Fig. 11). The dominant control of viscosity is temperature, as it has a much greater effect on the viscosity than pressure (Fig. 12). A decrease in viscosity from 0.2(1) mPa s to 0.13(5) mPa·s is observed with a temperature increase from 373 K to 473 K at 1.5 GPa. An initial decrease in room-temperature viscosity to 0.6(2) mPa·s when compressing the sample at room temperature to 207 MPa relative to ambient pressure viscosity of 1 mPa·s, is followed by an increase in viscosity to 2(2) mPa·s after further compression to 590 MPa (Fig. 13).   This behavior is a consequence of the low-pressure and temperature fluid structure variations responsible for many of the unique thermodynamic properties of water. At high pressures and high temperatures, however, H_2O is unlikely to undergo such dramatic structure fluctuations.

The data are consistent with an Arrhenius model for viscosity (eqn. 9; Fig. 14) for T/T_m between 1.07 and 1.54 with a best-fit η_0 = 2(2) Pa·s and g=7(1) which is related to the activation enthalpy.

Chapter 4

Discussion

4.1 Viscosity as a Function of *P* and *T*

The results from this study show clear pressure dependence at ambient temperature consistent with the decrease observed by *Bett and Cappi* [1965]. While the viscosity values derived from this study are all within 0.6 log units of the values of *Abramson* [*2007*], the *Abramson* [2007] data show a pressure dependent viscosity increase at higher temperatures and in the stability field of Ice VI and Ice VII. The rolling sphere method that was used in the *Abramson* [2007] study may be inaccurate when measuring low viscosities due to the rapid time over which the sphere traverses the sample chamber compounded by wall effects. At elevated temperatures, the method used in this study produces lower viscosities as compared to previously published values (Fig. 11; Fig. 14). The study published by *Dudziak and Frank* [1966] was conducted at relatively low pressures (<1 GPa) using an oscillating disc viscometer that may be influenced by large wall effects [*Newell,* 1959]. Also, previous studies that use a capillary-type viscometer can be subject to changes from laminar to turbulent flow which results in higher measured viscosities [*Nagashima and Tanishita,* 1969]. Due to the size of the particles relative to the size of the sample chamber, the Brownian motion method should be more sensitive to lower viscosities due to the decreased effect of wall drag. This reasoning explains why the previous studies show a deviation from a homologous temperature relationship and why the method of Brownian motion observation results in viscosities that confirm the homologous temperature dependence of water over the pressure and temperature range of this study.

Previous studies show that water viscosity deviates from both fixed-activation energy and fixed-activation volume Arrhenius models as well as the Doolittle and Vogel-Fulcher-Tammann (VFT) fitting equations [*Abramson, 2007*]. The VFT is suited for liquids as they approach the glass transition [*Garcia-Colin et al.,* 1989] and the free-volume models reproduce data for inorganic and organic glasses over a wide range of temperatures down to the glass-transition [*Courtney,* 2005]. An analogous experiment also by *Abramson* [2009] on supercritical carbon dioxide shows a viscosity-temperature-density relationship that is better described by a modified free-volume equation. The Doolittle and VFT are based on the free-volume model. The free volume model is based on the concept that in a fluid of hard spheres, statistical redistribution of the free-volume allows the structure to open up sufficiently for diffusion to occur [*Cohen and Turnbull,* 1959]. The free-volume concept can also be thought of as the separation of molecules whereas the resistance of molecules to flow, viscosity, past one another is dependent on this intermolecular separation [*Doolittle,* 1952]. However, at ambient conditions, water is a complex polymerization of H_2O molecules, but the diffusion and transport properties of water are more similar to a non-associated, unpolymerized liquid [*Sciortino et al.,* 1991]. Therefore, the Doolittle equation is more accurate at fitting data than for extrapolation or interpolation [*Doolittle and Doolittle*, 1957] and a better model that can account for the pressure and temperature dependence of viscosity is needed to allow for extrapolation to subduction zone conditions.

The IAPWS equations for pure water are only valid to pressures of 1 GPa and are not suited for other pressures [*Huber et al,* 2009]. Also, the IAPWS is based on global fits of experimental data and thus may also be influenced by experimental error caused by wall effects.

When the results presented in this study are normalized to the high pressure melting temperature calculated from the equations of *Choukron and Grasset* [2007] and *Lin et al.* [2004] (Fig. 14), the results are comparable to experiments conducted at 0.1 MPa up to the boiling point [*Aleksandrov and Trakhtengerts,* 1976] and are therefore consistent with a homologous temperature relationship. Fitting the 0.1 MPa data of *Aleksandrov and Trakhtengerts* [1976] using equation (**9**) yields values of η_0 = 0.50(5) and g=5.7(1). These values are consistent within experimental uncertainty to values of η_0 = 2(2) Pa·s and g=7(1) determined in these high-pressure experiments.

Even though the data are in agreement with previous experiments at low homologous temperatures, $T/T_m > 1.5$ needs to be considered to discuss subduction zone processes. The higher exponential constant determined from these results, therefore, predict lower viscosities at higher homologous temperatures than the 0.1 MPa model. The resulting homologous temperature models, however, do not fit previous experimental data [*Dudziak and Frank*, 1966; *Abramson*, 2007] at high values of T/T_m. (Fig. 14) Furthermore, comparable experiments on nitrogen and carbon dioxide in the supercritical state also show a deviation from the homologous temperature relationship [*Abramson,* 2008; *Abramson*, 2009]. The asymptotic behavior of water (and CO_2 and N_2) viscosity at high homologous temperatures is likely due to the difficulty in measuring very low viscosities ($< 10^4$ Pa·s) with the sliding sphere method.

The Brownian motion approach is therefore more suitable to the sample size of the diamond anvil cell allowing for measurement of lower viscosities in order to elucidate the transport properties of water in subduction zones. Even though the Brownian motion method in the DAC reduces the effect of wall drag, there are other uncertainties that need to be taken into account. A 7% uncertainty in the pixel dimension (Table 2) can result in a 33% uncertainty in the viscosity calculated from tracking one particle for 20 seconds in a low ($<10^{-4}$ Pa·s) viscosity fluid. Uncertainty in the radius of the particle contributes a ~3% uncertainty in the measured apparent viscosity assuming that the radius of the particle does not change significantly during the experiment. The particle size does not change within the resolution of the image in our experiments. The temperature measurements contribute much less than 1% to uncertainty in viscosity, however the temperature at which the phase change occurs results in a ~5% uncertainty in the homologous temperature. The wall correction calibration uncertainty contributes another 18% to the uncertainty in the calculated viscosity. Greater accuracy arises by tracking more particles per sample. However, the concentration of particles in suspension also plays an important role, as there appears to be an optimal concentration of ~10-20 particles in the focal plane. With too many particles, the particle—particle interaction will lead to bias overestimating viscosity. If the number of particles is too small, then there are fewer particles to provide a reasonable average.

4.2 Implications for Subduction

Water released at ~100 km depth is firmly in the supercritical field, more than 2 log units past the critical pressure and temperatures up to a factor of 2 past the critical temperature. There is uncertainty in extrapolating measurements made on liquid water to the properties of supercritical H_2O. Above the critical point, water behaves as a supercritical fluid. The viscosity of a gas tends to increase with increasing temperature and tends to decrease for liquids. The material properties of a supercritical fluid are somewhere between that of a gas and a liquid and therefore diverge asymptotically at the critical point. The divergence at the critical point is associated with large density fluctuations [*Huber et al.*, 2009]. At the critical point, T=647.096 K and P=22.064 MPa, a fluid has infinite viscosity [*Huber et al.*, 2009] because of macroscopic density fluctuations leading to theoretically infinite compressibility. Such large fluctuations in the density of water will alter the strength and type of hydrogen bonding and therefore affect the compressibility of the fluid. Fluctuations in compressibility near the critical point may cause viscosity fluctuations at the critical point and asymptotic behavior. However, these large fluctuations are only significant near the critical point. The fluids released during slab dehydration should be far enough beyond the critical point to maintain a stable structure and therefore the viscosity should conform to a homologous temperature model.

Hydrofracturing models predict much less than 1 year for the fluid to be transported out of the slab and into the mantle wedge assuming the viscosity of pure water at ambient conditions. Alternatively, porous flow of fluids through the mantle wedge would require more than 2 x 10^{10} years if a pure water viscosity of 100µPa·s is assumed based on low pressure, high temperature behavior [*Dudziak and Franck*, 1966]. Experimental diffusion coefficients for olivine yield timescales of 10^6 years for transport over distances of ~10-60 m via lattice or grain boundary diffusion, respectively [*Demouchy and Mackwell*, 2006; *Kohlstedt and Mackwell*, 1998; *Demouchy,* 2010] assuming reasonable grain sizes. If the mantle wedge olivine is saturated with water due to dehydration reactions then the transport of hydrogen via grain-boundary diffusive flow can be significant with timescales of 10^6 years for a lengthscale of 4 km [*Demouchy*, 2010].

Based on the homologous temperature model presented here, the viscosity of pure water will decrease by more than 4 log units when heated to 1273 K and compressed to 3.6 GPa (Fig. 15), assuming the homologous temperature relationship holds into the supercritical stability field. Because the supercritical field will likely have a higher viscosity, the homologous model is a firm lower bound for the viscosity of water released from a subducted slab. Due to the corrosive behavior of supercritical water, aqueous fluids released from slabs are likely highly enriched in silica incorporated from mantle rock. 80 wt% dissolved silica has been shown to increase the viscosity of pure water by 5 orders of magnitude at 1073 K [*Audetat and Keppler*, 2004]. In an attempt to reconcile the rapid ascent rates of material from the slab to the surface that are suggested from geochemical data, end member constraints of pure water and an aqueous fluid with 80% dissolved silicate for both a cold and hot slab thermal regime, 673 K and 1273 K at 115 km depth [*Kincaid and Sacks*, 1997] encapsulate the range of viscosities for all relevant conditions.

One can express the velocity of a fluid flowing vertically through porous media [*Turcotte and Schubert,* 2002] as:

$$v = \frac{-k}{\eta}\left(\frac{dp}{dy} - \rho g\right) \qquad \textbf{(10)}$$

where v is the fluid velocity, k is the permeability of the mantle rock, η is the viscosity of the fluid, dp/dy is the pressure gradient due to self-compression of mantle rock, g is the acceleration due to gravity and ρ is the density of the fluid. Assuming that mantle rock is extremely impervious, we can use k=10^{-21} m^2 along with dp/dy of 30 MPa/km

[*Dziewonski and Anderson*, 1981] and a liquid density of 1.4 x 10^3 kg/m^3 [*Wiryana et al*., 1998]. Based on these calculations, it will take 20,000 years for pure water to travel just 1 m from a cold slab. Pure water released from a hot slab will ascend via porous flow much more rapidly but will still take 10^7 years to travel 50 km into the mantle wedge. If one considers the effect of tortuosity then the transport time will be even slower resulting in a further deviation from the geochemical observations.

Fluid flow through cracks can be modeled as [*Philpotts*, 1990]

$$\bar{v} = \frac{-1}{12\eta}\left(\rho_f - \rho_r\right)W^2 \tag{12}$$

where v is the average flow velocity, ρ_f is the density of the fluid, ρ_r is the density of the rock, and W is the width of the crack. Assuming a crack width of 0.01m-0.2m [[*Davies*, 1999], then the flow rates of pure water with the appropriate cold-slab water viscosity are ~1.7 km/s for a 10mm wide crack and >600 km/s for a 200 mm wide crack, both of which are physically unreasonable. These velocities are based on the assumption the flow is purely laminar. Pure water flowing from a cold-slab through a crack 10 mm wide will travel 50 km into the mantle wedge in less than 1 minute. The velocities of pure water, based on these calculations, flowing from a hot slab are in even higher. These velocities are based on the assumption the flow is purely laminar. These unreasonably, high velocities show that flow of water in the mantle wedge must be turbulent and thus subject to friction from surface roughness. Also, these extremely high flow velocities show that the cracks formed during dehydration of subducted slabs must be much less than 10mm in width and fluid may by flowing through a large number of microcracks with very small apertures as opposed to larger channels. The flow velocities through a crack are highly dependent on the crack width. Decreasing the crack width by 2 orders of magnitude will decrease the velocity by 4 orders of magnitude which will yield more reasonable, yet still rapid timescales. The rapid timescales associated with hydrofracturing due to the expected decrease in the viscosity of water is consistent with the rapid transport of material from the subducted plate to the surface inferred from geochemical observations.

However, we need to consider the effect of silicate dissolution due to the supercritical behavior of water at these conditions. At 1073 K, *Audetat and Keppler* [2004] found that for 80 wt% dissolved silica the viscosity increases by 5 orders of magnitude from that of pure water. If the viscosities predicted from the homologous temperature relationship are increased by this amount, then it would take less than 9 hours for the fluid released from a hot slab to flow 50 km through 10 mm wide cracks and induce partial melting. If flow of silica-rich aqueous fluids from a cold slab is the dominant mechanism of transport, then it will take less than ~ 3 months for fluid to reach the surface.

The results from this study are consistent with geochemical observations. Slab dehydration can produce H_2O-saturated fluids with low viscosities that are rapidly transported to the mantle-melting source region within the available timescales predicted from geochemical observations. Additional time needed to reconcile the geochemical observations can be accounted for by the time needed for ascent of the H_2O-saturated mantle, melting of the mantle and segregation of the melt, ascent of the melt, storage in a crustal chamber, and finally eruption at the surface.

A decrease in pure water viscosity of more than two orders of magnitude at high pressures and high temperatures may support the hypothesis set forth by *Petford et al.*, [2008]. Their model of melt transport in the overlying mantle wedge is a combination of initial porous flow followed by flow through dilating channels. This two stage flow is needed to account for the timescales associated with the ^{226}Ra-^{210}Pb disequilibria. The rate of fluid flow via percolation through porous media is dependent upon the viscosity (eqn. 10). These new results from this study show that the viscosity of water, a crucial component in estimating melt viscosities in the mantle wedge, is not constant over a wide range of homologous temperatures.   The experimental values of water viscosity at high pressures and high temperatures from this study may be extrapolated to subduction zone conditions and potentially be used in more robust geodynamic models that account for the complex thermal structure and kilometer-scale thermal gradients found in the mantle wedge. The models can then verify a combination of hydrofracturing and porous flow along with the role of diffusion in what is likely multi-stage, multi-phase flow to allow for a better comparison with the geochemical observations.

Chapter 5

Conclusions

A new method for measuring the viscosity of fluids in the hydrothermal diamond anvil cell has been developed. The method of Brownian motion observation reduces the effect of viscous wall drag and is more suitable for the small samples used in high-pressure experiments. Using Brownian motion, viscosities of water lower than previous diamond anvil cell experiments were measured. The results confirm a homologous temperature dependence of water viscosity up to T/T_m=1.5. This homologous temperature relationship coupled with assumptions about the effect of silica can be used to approximate the viscosity of subducted slab-derived fluids. Enrichment of silica has more of an effect on viscosity than temperature at subduction zone conditions. Based on these predictions, flow through microcracks produced by hydrofractruing can account for the rapid material transport times in subduction zones. In order to explain geochemical data, a combination of porous flow with flow through cracks or channels is likely necessary.

References

Abramson, E.H. (2005), The shear viscosity of supercritical oxygen at high pressure, *J. Chem. Phys., 122,* 084501.

Abramson, E.H. (2007), Viscosity of water measured to pressures of 6 GPa and temperatures of 300 C, *Phys. Rev. E, 76,* 051203.

Abramson, E.H. (2008), Viscosity of nitrogen measured to pressures of 7 GPa and temperatures of 573 K, *Phys. Rev. E., 77,* 041202.

Abramson, E.H. (2009), Viscosity of carbon dioxide measured to a pressure of 8 GPa and temperature of 673 K, *Phys. Rev. E, 80,* 021201.

Aleksandrov, A.A. and M.S. Trakhtengerts (1976), Viscosity of water at temperatures of -20 to 150 °C, *J. Eng. Phys. Thermophys., 27* (4), DOI: 10.1007/BF00864022.

Arcay, D., E. Tric, and M.-P. Doin (2005), Numerical simulations of subduction zones; Effect of slab dehydration on the mantle wedge dynamics, *Phys. Earth Planet. Int., 149,* 133-153.

Audetat, A., and H. Keppler (2004), Viscosity of fluids in subduction zones, *Science, 303,* 513-516.

Bassett, W.A., A.H. Shen, M. Bucknum, and I-M. Chou (1993), Hydrothermal studies in a new diamond anvil cell up to 10 GPa and from -190˚C to 1200˚C, *Pure Appl. Geophys*., 141 (2-4), 487-495.

Bett, K.E., and J.B. Cappi (1965), Effect of pressure on the viscosity of water, *Nature, 207,* 620-621.

Chijioke, A.D., W.J. Nellis, A. Soldatov, and I.F. Silvera (2005), The ruby pressure standard to 150 GPa, *J. App. Phys., 98,* 114905.

Choukroun, M., and O. Grasset (2007), Thermodynamic model for water and high-pressure ices up to 2.2 GPa and down to the metastable domain, *J. Chem. Phys., 127,* 124506.

Cohen, M.H., and D. Turnbull (1959), Molecular transport in liquids and glasses, *J. Chem. Phys., 31* (5), 1164-1169.

Cook, R.L., H.E. King, Jr., and D.G. Peiffer (1992), High-pressure viscosity of dilute polymer solutions in good solvents, *Macromolecules, 25,* 2928-2934.

Courtney, T.H. (2000), *Mechanical Behavior of Materials,* 2nd ed., McGraw Hill, Boston.

Crocker, J. (1997), Measurement of the hydrodynamic corrections to the Brownian motion of two colloidal spheres, *J. Chem. Phys., 106* (7), 2837-2840.

Davies, J.H., The role of hydraulic fractures and the intermediate-depth earthquakes in generating subduction-zone magmatism, *Nature, 398*, 142-145, 1999.

Demouchy, S., and S.J. Mackwell (2003), Water diffusion in synthetic iron-free forsterite, *Phys. Chem. Minerals, 30,* 486-494.

Demouchy, S., and S.J. Mackwel (2006), Mechanisms of hydrogen incorporation and diffusion in iron-bearing olivine, *Phys. Chem. Miner., 33,* 347-355.

Demouchy, S. (2010), Diffusion of hydrogen in olivine grain boundaries and implications for the survival of water-rick zones in the Earth's mantle, *Earth Planet. Sci. Lett.,295,*305-313.

Doolittle, A.K. (1952), Studies in Newtonian flow. III. The dependence of the viscosity of liquids on molecular weight and free space (in homologous series), *J. Appl. Phys., 23* (2), 236-239.

Doolittle, A.K., and D.B. Doolittle (1957), Studies in Newtonian flow. V. Further verification of the free-space viscosity equation, *J. Appl. Phys., 28* (8), 901-905.

Dudziak, K.H. and E.U. Franck (1966), Messungen der Viskositat des Wassers bis 560 °C und 3500 bar, *Ber. Bunsenges. Phys. Chem., 70,* 1120-1128.

Dufresne, E., D. Altman, and D. Grier (2001), Brownian dynamics of a sphere between parallel walls, *Europhys. Lett., 53,* 264-270.

Dziewonski, A.M., and D.L. Anderson (1981), Preliminary reference Earth model, *Phys. Earth Planet. Int., 25,* 297-356.

Einstein, A. (1926), *Investigations on the theory of Brownian movement*, Methuen & Co. ltd., London.

Faccenda, M., T.V. Gerya, and L. Burlini (2009), Deep slab hydration induced by bending-related variations in tectonic pressure, *Nature Geosci., 2* (11), 790-793, doi: 10.1038/NGEO656.

Garcia-Colin, L.S., L.F. del Castillo, and P. Goldstein (1989), Theoretical basis for the Vogel-Fulcher-Tammann equation, *Phys. Rev. B , 40* (10), 7040-7044.

Grocholski, B. and R. Jeanloz (2005), High-pressure and –temperature viscosity measurements of methanol and 4:1 methanol:ethanol solution, *J. Chem. Phys., 123*, 204503.

Grant. I. (1997), Particle image velocimetry: A review, *Proceedings of the Institution of Mechanical Engineers Part C- Journal of Mechanical Engineering Science, 211* (1), 55-76.

Hacker, B.R., S.M. Peacock, G.A. Abers, and S.D. Holloway (2003), Subduction factory 2. Are intermediate-depth earthquakes in subducting slabs linked to metamorphic dehydration reactions*?, J. Geophys. Res., 108* (B1), 2030, doi:10.1029/2001JB001129.

Huber, M.L., R.A. Perkins, A. Laesecke, D.G. Friend, J.V. Sengers, M.J. Assael, I.N. Metaxa, E. Vogel, R. Mares, K. Miyaga (2009), New International Formulation for the Viscosity of H_20, *J. Phys. Chem. Ref. Data, 38 (2),* 101-125.

Iwamori, H. (1998), Transportation of H_2O and melting in subduction zones, *Earth Planet. Sci. Lett., 160,* 65-80.

Irifune, T. (1987), An experimental investigation of the pyroxene – garnet transformation in a pyrolite composition and its bearing on the constitution of the mantle, *Phys. Earth. Planet. Int., 45,* 324-336.

Kahle, A., B. Winkler, and B. Hennion (2003), Is Faxén's correction function applicable to viscosity measurements of silicate melts with the falling sphere method?, *J. Non-Newtonian Fluid Mech. 112*, 203–215.

Kell, G.S. (1975), Density, thermal expansivity, and compressibility of liquid water from 0° to 150°C: Correlations and tables for atmospheric pressure and saturation reviewed and expressed on 1968 temperature scale, *J. Chem. Eng. Data, 20* (1), 97-105.

Kincaid, C., and Sacks, I.S. (1997), Thermal dynamical evolution of the upper mantle in subduction zones, *J. Geophys. Res., 102* (B6), 12,295-13,315.

King, H.E., E. Herbolzheimer, and R. L. Cook (1992), The diamond-anvil cell as a high-pressure viscometer, *J. Appl, Phys., 71* (5), 2071-2081.

Kohlstedt, D.L., and S.J. Mackwell (1998), Diffusion of hydrogen and intrinsic point defects in olivine, *Z. Phys. Chem., 207,* 147-162.

Lin, J., B. Militzer, V. V. Struzhkin, E. Gregoryanz, R. J. Hemley, and H. Mao (2004), High pressure-temperature Raman measurements of H_2O melting to 22 GPa and 900 K, *J. Chem. Phys., 121* (17), 8423-8427.

Meade, C., and R. Jeanloz (1991), Deep-focus earthquakes and recycling of water into the Earth's mantle, *Science, 252,* 68-72.

Mibe, K., T. Fujii, and A. Yasuda, Control of the location of the volcanic front in island arcs by aqueous fluid connectivity in the mantle wedge, *Nature, 401*, 259-262, 1999.

Mibe, K., T. Yoshino, S. Ono, A. Yasuda, and T. Fujii (2003), Connectivity of aqueous fluid in eclogite and its implications for fluid migration in the Earth's interior, *J. Geophys. Res., 108* (B6), 2295, doi: 10.1029/2002JB001960.

Mukai, S.-a., S. Deguchi, and K. Tsujii (2006), A high-temperature and –pressure microscope cell to observe colloidal behaviors in subcritical and supercritical water: Brownian motion of colloids near a wall, *Colloid. Surface. A, 282-283,* 483-488, doi:10.1016/j.coisurfa.2005.10.048.

Nagashima, A., and I. Tanishita (1969), Viscosity measurement of water and steam at high temperatures and high pressures, *Bull. Jap Soc. Mech. Eng.,12* (54), 1467-1478.

Newburgh, R., J. Peidle, and W. Rueckner (2006), Einstein, Perrin, and the reality of atoms: 1905 revisited, *Am. J. Phys.*, *74, (6),* 478-481.

Newell, G.F. (1959), Theory of oscillation type viscometers V: Disk oscillating between fixed plates, *Z. Angew. Math. Phys.**,** 10* (2),160-174, doi: 10.1007/BF01600523.

Padron-Navarta, J.A., A. Tommasi, C.J. Garrido, V.L. Sanchez-Vizcaino, M.T. Gomez-Pugnaire, A. Jabaloy, and A. Vauchez (2010), Fluid transfer into the wedge controlled by high-pressure hydrofracturing in the cold top-slab mantle, *Earth Planet. Sci. Lett.,297,* 271-286.

Petford, N., M. A. Koenders, and S. Turner (2008), Channelized melt flow in downwelling mantle: Implications for ^{226}Ra-^{210}Pb disequilibria in arc magmas, *J. Geophys, Res., 113,* B11202, doi: 10.1029/2007JB005563.

Poirer, J.P. (1988), Transport properties of liquid metals and viscosity of the Earth's core, *Geophys. J. Int., 92*, 99-105.

Poirer, J.-P. (2000), *Introduction to the physics of the Earth's interior,* Cambridge University Press, Cambridge.

Raleigh, C.B., and M.S. Paterson (1965), Experimental deformation of serpentinite and its tectonic implications, *J. Geophys. Res.*, *70*(16), 3965.

Richard, G., M. Monnereau, and M. Rabinowicz (2007), Slab dehydration and fluid migration at the base of the upper mantle: implications for deep earthquake mechanisms, *Geophys. J. Int., 168,* 1291-1304.

Schiller, L. (1931), *Hydro- and Aerodynamik; 1. Teil Strömungslehre und allgemeine Versuchstechnik* (Akademische Verlagsgesellschaft M.B.H., Leipzig).

Schiller, L. (1932), *Hydro- und Aerodynamik; 2. Teil Widerstand und Auftrieb* (Akademische Verlagsgesellschaft M.B.H., Leipzig).

Schmidt, M.W., and S. Poli (1998), Experimentally based water budgets for dehydrating slabs and consequences for arc magma generation, *Earth Planet. Sci. Lett., 163,* 361-379.

Sciortino, F., A. Geiger, and H.E. Stanley (1991), Effect of defects on molecular mobility in liquid water, *Nature, 354,* 218-221.

Sigmarsson, O., J. Chmeleff, J. Morris, and L. Lopez-Escobar (2002), Origin of ^{226}Ra-^{230}Th disequilibria in arc lavas from southern Chile and implications for magma transfer time, *Earth Planet. Sci. Lett., 196,* 189-196.

Terasaki, H., T. Kato, K. Funakoshi, A. Suzuki, and S. Urakawa (2004), Viscosity of liquid sulfur under high pressure, *J. Phys.-Condens. Mat., 16,* 1707-1704.

Turcotte, D. L., and G. Schubert (2002), *Geodynamics*, 2nd ed., Cambridge University Press, New York.

Turner, S., and C. Hawkesworth (2001), Constraints on flux rates and mantle dynamics beneath island arcs from Tonga-Kermadec lava geochemistry, *Nature, 389*, 568-573.

van Keken, P.E. (2003), The structure and dynamics of the mantle wedge, *Earth Planet. Sci. Lett.,215*, 323-338.

Wilke, M., K. Appel, L. Vincze, C.Schmidt, M. Borchert, and S. Pascarelli (2010), A confocal set-up for micro-XRF and XAFS experiments using diamond-anvil cells, *J. Synchrotron Radiat.,17,* 669-675, doi: 10.1107/S0909049510023654.

Wiryana, S., L.J. Slutsky, and J.M. Brown (1998), The equation of state of water to 200˚C and 3.5 GPa: model potentials and the experimental pressure scale, *Earth Planet. Sci. Lett.,163,* 123-130.

Appendix A: Tables and Figures

Experiment No.	**Pre-heat P (GPa)**	**P_m (GPa)**	**P_c (GPa)**	**Post-heat P (GPa)**	**T (K)**	**P_{ref} (GPa)**	**ΔT**	**P_{th} (GPa)**	**P_{tot} (GPa)**
3529	6.66	3.98	2.76	3.14	523	2.76	110	0.07	2.83
3539	1.38	2.03	1.48	1.39	373	1.48	47	0.03	1.51
3540	1.38	2.03	1.48	1.39	423	1.48	97	0.06	1.54
3541	1.38	2.03	1.48	1.39	473	1.48	137	0.09	1.57
3575	2.38	3.15	n.a.	0.92	463	0.92	170	0.1	1.02
3627	2.63	2.2	n.a.	0.4	100	0.4	81	0.05	0.45

Table 1: Pressure and temperature conditions for all of the high-temperature experiments. The pre-heat and post-heat P values were obtained using the ruby fluorescence method at room temperature [*Chijoke et al.*, 2005]. P_m and P_c are the inferred pressures of melting and crystallization upon heating and cooling and based on the melting curves of H_2O [*Choukroun and Grasset*, 2007*; Lin et al.*, 2004*;* Figure 3]. T is the temperature at which the viscosity measurement was made and P_{th} is contribution from thermal pressure at ΔT above P_{ref} such that the total pressure of the experiment is inferred as P_{tot}. If the liquid-solid phase transition was not observed upon cooling, P_c is listed as not available (n.a.).

Experiment No.	**P (GPa)**	**T (K)**	**t (s)**	**Particles**	**dpix (µm)**	**Thickness (µm)**
3383	0.12	294	30.1	6	0.9(0.2)	140
3384	0.26	294	30.1	2	0.9(0.2)	140
3385	0.21	294	30.1	6	0.9(0.2)	140
3386	0.23	294	30.1	6	0.9(0.2)	140
3529	2.83	523	29.7	6	0.57(5)	30
3539	1.51	373	20.3	5	0.59(4)	59
3540	1.54	423	28.6	5	0.59(4)	59
3541	1.57	473	21.3	5	0.59(4)	59
3575	1.02	463	19.5	5	0.59(3)	83
3623	0.25	292	40	6	0.61(4)	40
3624	0.59	292	40	6	0.61(4)	30
3627	0.45	373	40	6	0.61(4)	30

Table 2: Experimental conditions for all experiments conducted above ambient pressure and temperature. *P* and *T* are the pressure and temperature respectively at the time of viscosity measurement, *t* is the time in seconds of the video analyzed for MSD, and *dpix* is the pixel dimension reflecting variations in camera magnification between experiments. The thickness of the gasket for the viscosity measurements and the number of particles tracked during each experiment are also listed. The uncertainty in *dpix* is 1σ.

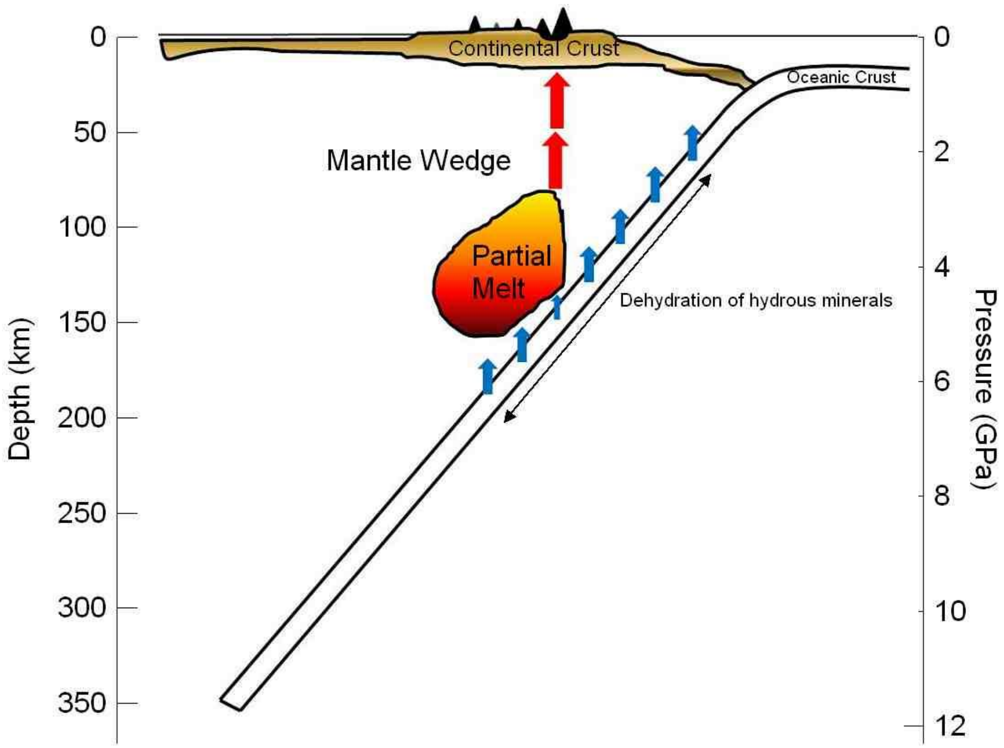

Figure 1: Cross-section of a subduction zone adapted from *Schmidt and Poli* [1998]. Dehydration of hydrous minerals (blue arrows) contained in the dense oceanic crust (white) below continental crust (brown) leads to partial melting (reddish-yellow) of the mantle wedge which buoyantly rises (red arrows) to the surface leading to arc volcanoes (black triangles).

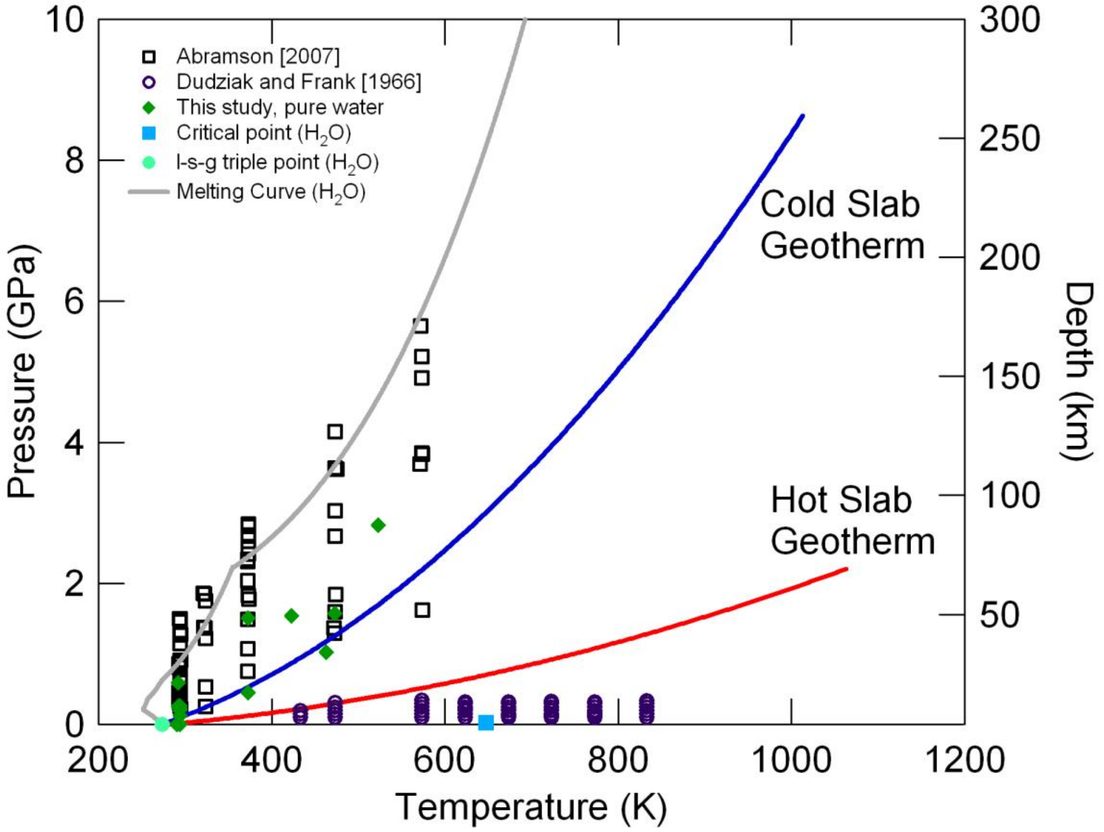

Figure 2: Pressures and temperatures of available experimentally derived pure water viscosity data relevant to subduction zones. Open black squares are data from *Abramson* [2007], open purple circles are from *Dudziak and Frank* [1966] and green diamonds are data from this study. The light green circle represents the solid-liquid-vapor triple point of water and the blue square is the critical point of water. Solid lines represent the range of *P-T* paths for subducting slabs [*Kincaid and Sacks, 1997*] for young and fast slabs (red) and old and slow slabs (blue) and the melting curve of water (gray) [*Choukroun and Grasset*, 2007; *Lin et. al.*, 2004]

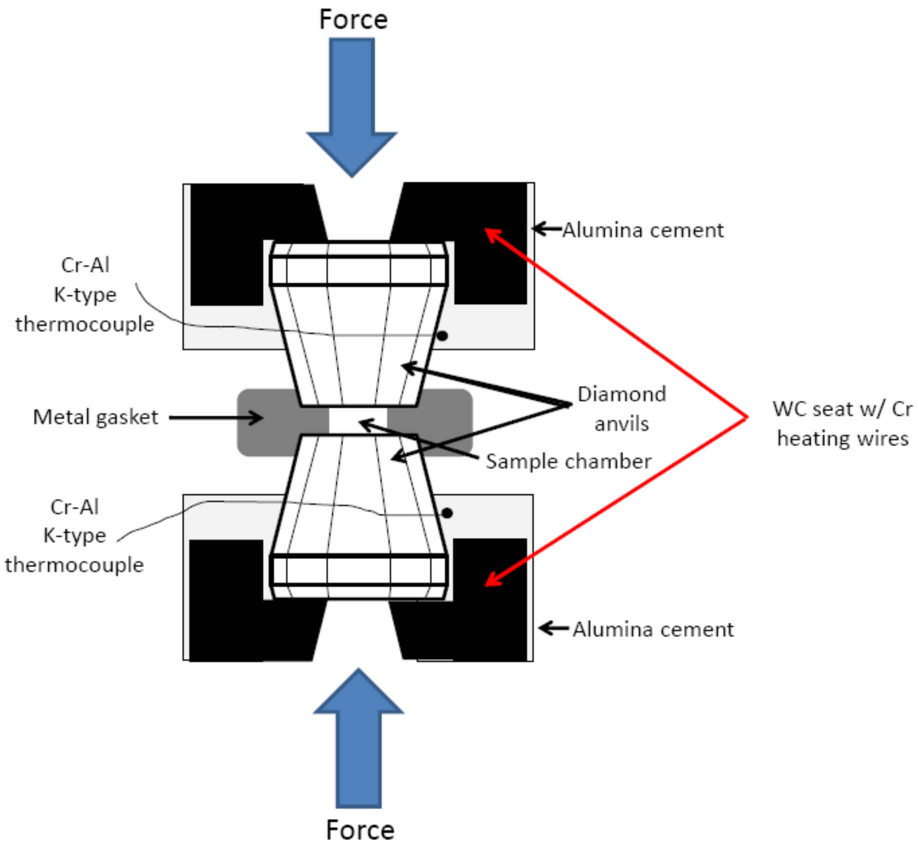

Figure 3: Schematic cross-section of the HDAC. The sample (labeled) is contained in a metal gasket (dark gray) and compressed uniaxially by applying a force to the top and bottom diamond anvils (labeled). The diamond anvils rest on tungsten carbide seats (black). The sample is heated from the top and bottom using chromel heating wires (labeled) wrapped around the WC seats. Temperature is measured using K-type chromel-alumel thermocouples (labeled) which are wrapped around both the top and bottom anvils. The diamonds are secured to the seat and the thermocouples are secured around the diamonds using alumina cement (light gray).

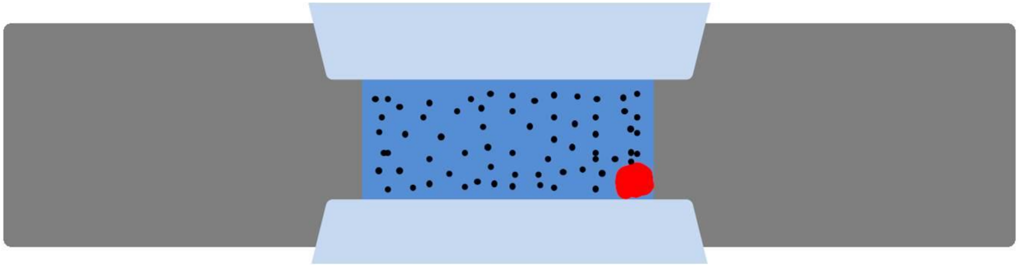

Figure 4: Schematic cross-section of the sample contained in the DAC. Gray represents the metal gasket, light blue represents the diamond anvils, dark blue is H_2O, red represents the Cr-doped ruby chip for pressure measurements, and small black circles are the polystyrene microspheres.

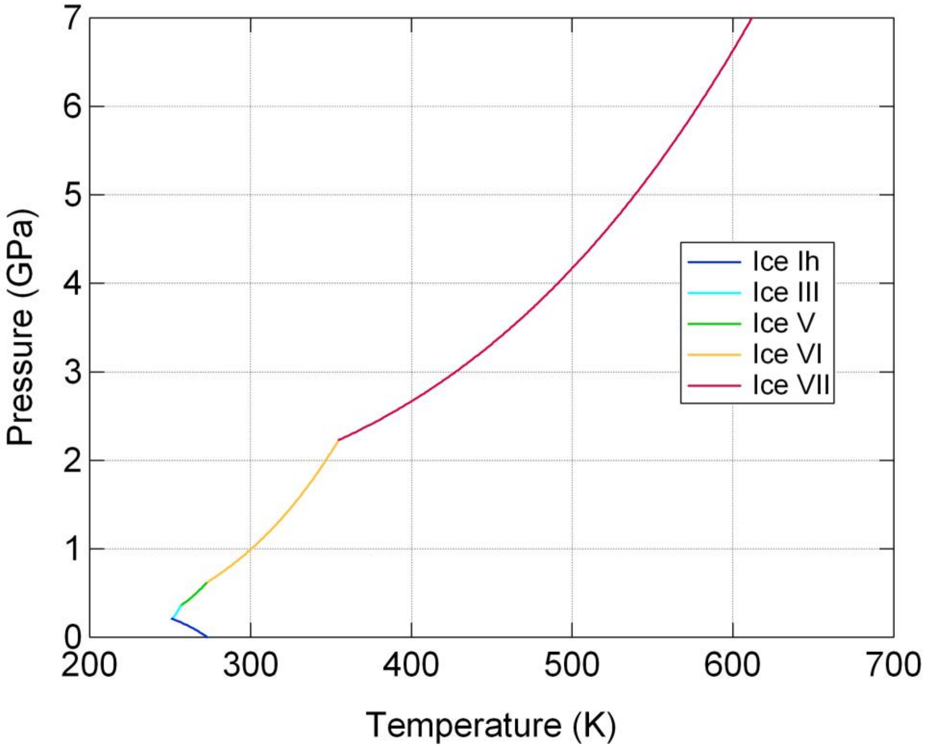

Figure 5: Diagram showing the melting curve of the ice phases relevant to the pressures and temperatures of this study. The Ice 1h, Ice 3, Ice 5, and Ice 6 curves were calculated from a thermodynamic model [*Choukroun and Grasset*, 2007]. The Ice VII curve was calculated from experimental melting data [*Lin et. al.*, 2004].

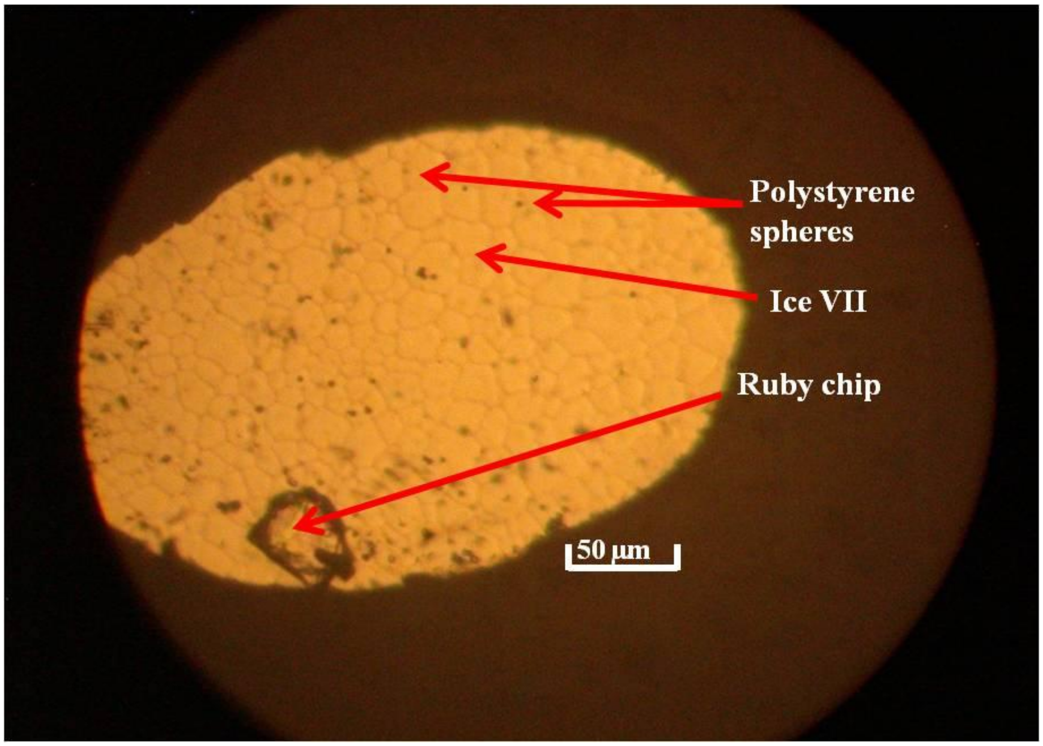

Figure 6: HDAC loaded with water-polystyrene sphere suspension and a ruby. At the end of the experiment, the water has frozen upon cooling forming ice crystals. Crystallization occurred at 413 K which corresponds to a pressure along the melting curve of 2.8 GPa and is consistent with a post-heating ruby pressure of 3.1 GPa. These pressures suggest the formation of Ice-VII (labeled).

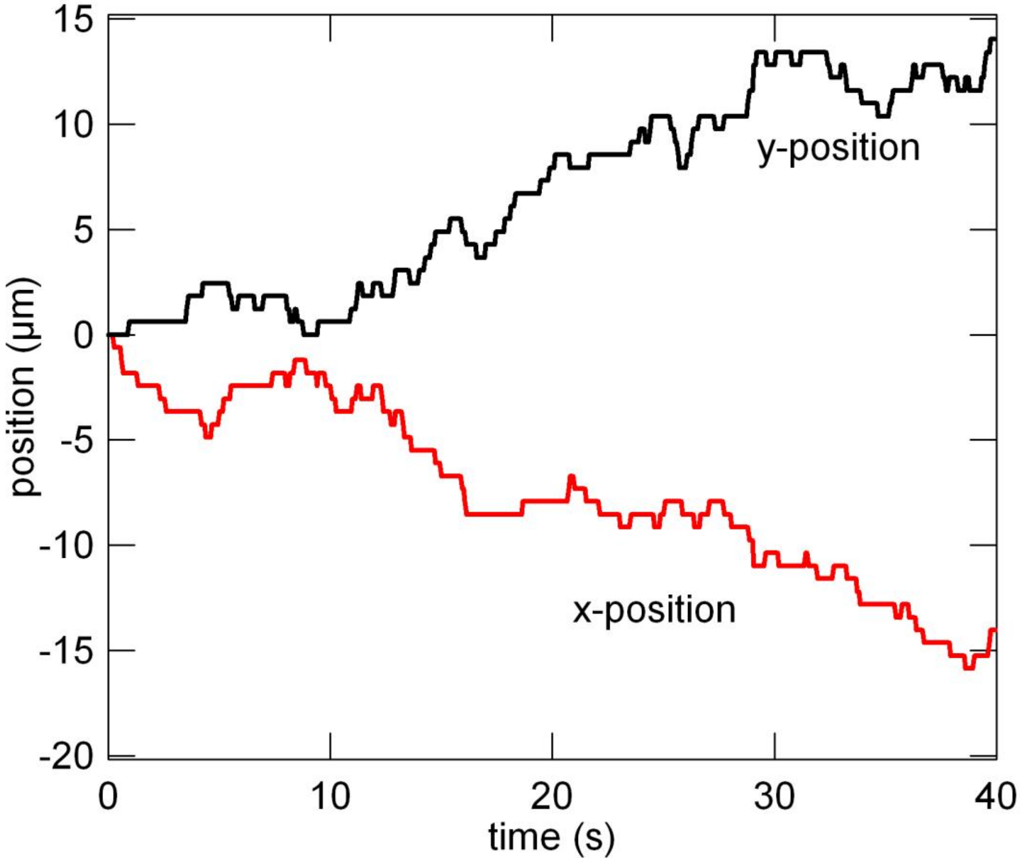

Figure 7: A comparison of the vector positions of a polystyrene sphere suspended in water within a HDAC at 0.4 GPa and 373 K. Position of the particle was generated by an automated particle-tracking velocimetry MATLAB program.

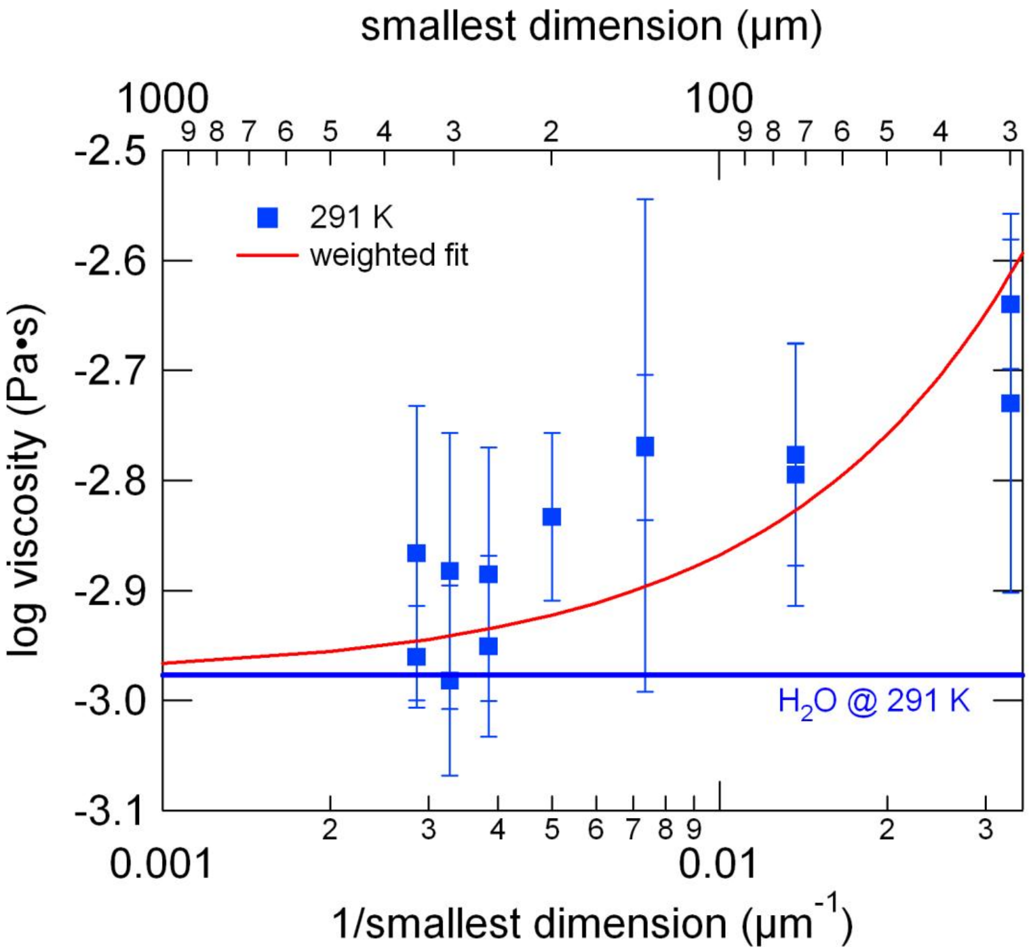

Figure 8: The effect of gasket thickness and gasket circumference shows that edge effects do not significantly affect the measurement for gasket dimensions greater than ~250 µm. For gasket thicknesses less than this, a correction is made to account for wall effects. The solid blue line is taken to be the true viscosity [*Aleksandrov and Trakhtengerts*, 1976]. The solid red line is a fit weighted according to the uncertainties in viscosity measurements.

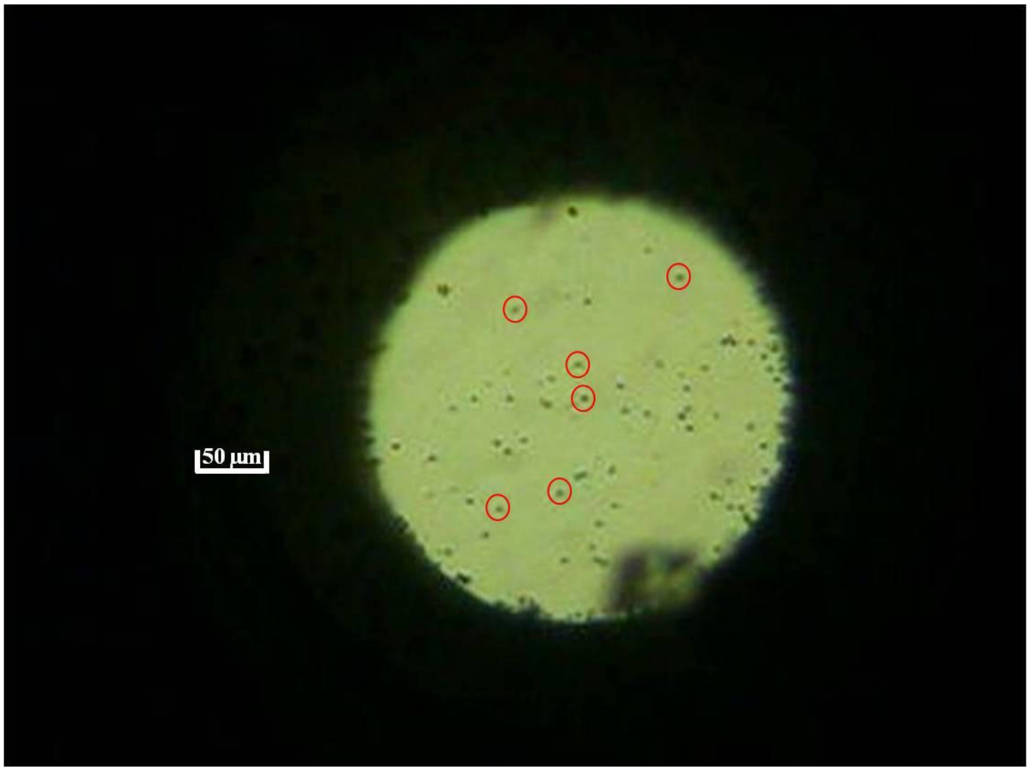

Figure 9: Frame 1 of the digitally recorded video used for the particle tracking routine. The sample was compressed to 0.2 GPa at 294 K. The red circles highlight those particles tracked used for viscosity measurements. These particles exhibited Brownian motion and were not observed to approach other particles throughout the measurement.

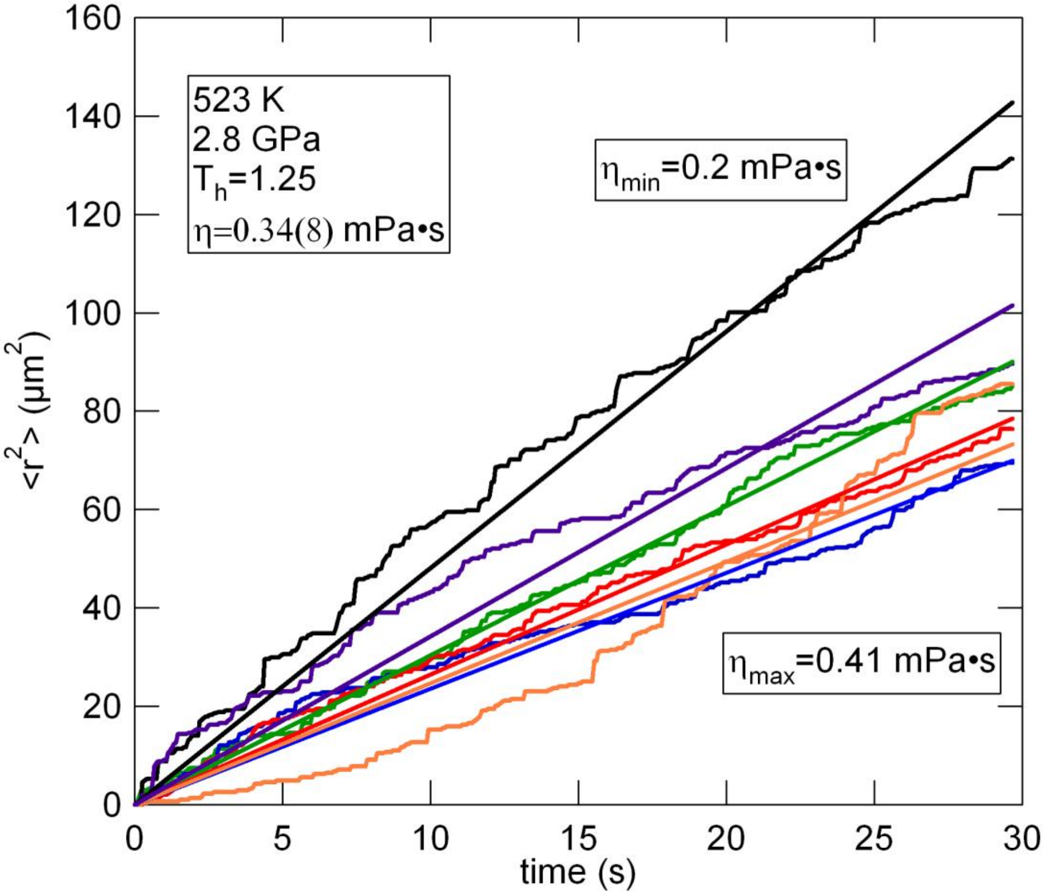

Figure 10: MSD as a function of time for 6 individual particles suspended in water at 2.8 GPa and 523 K. The maximum and minimum viscosities inferred from individual particles, η_{max} and η_{min} respectively are labeled.

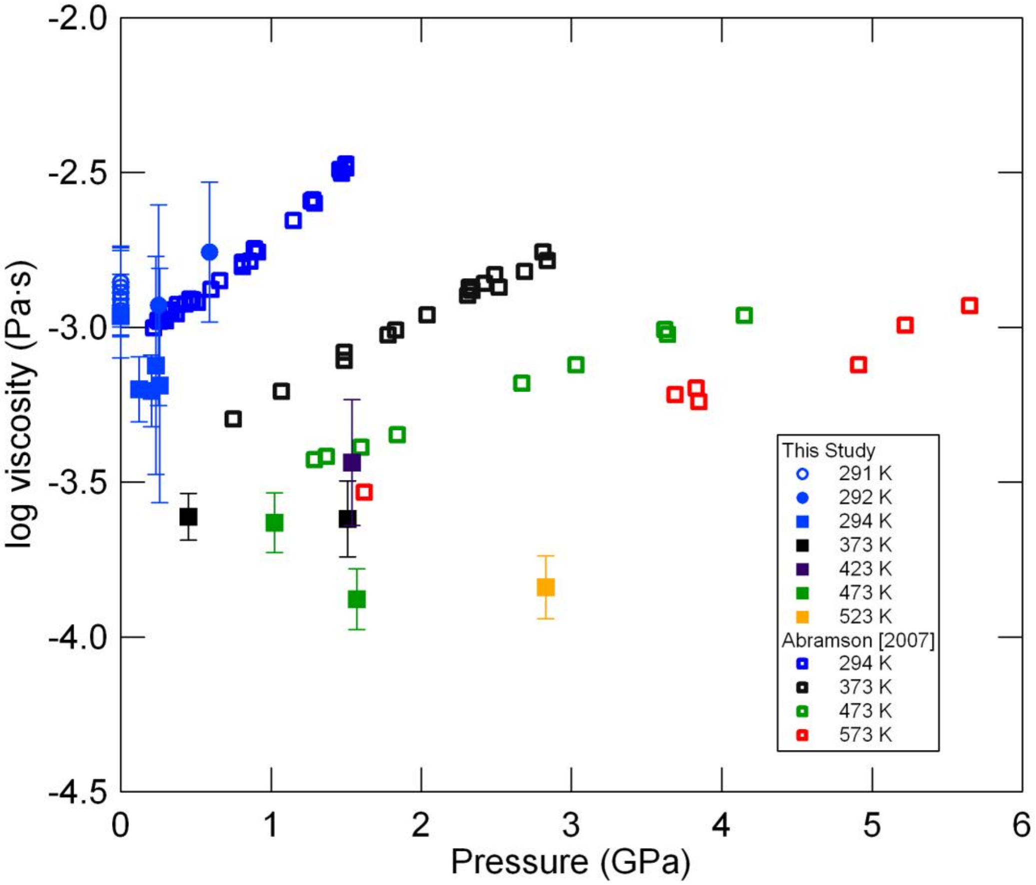

Figure 11: Viscosity as a function of pressure of experimental data from this study compared with published experimental data [*Abramson, 2007*]. The viscosity values from this study represent the average value of the single particle viscosities weighted according to the uncertainties in the slopes. The error bars represent 1 standard deviation.

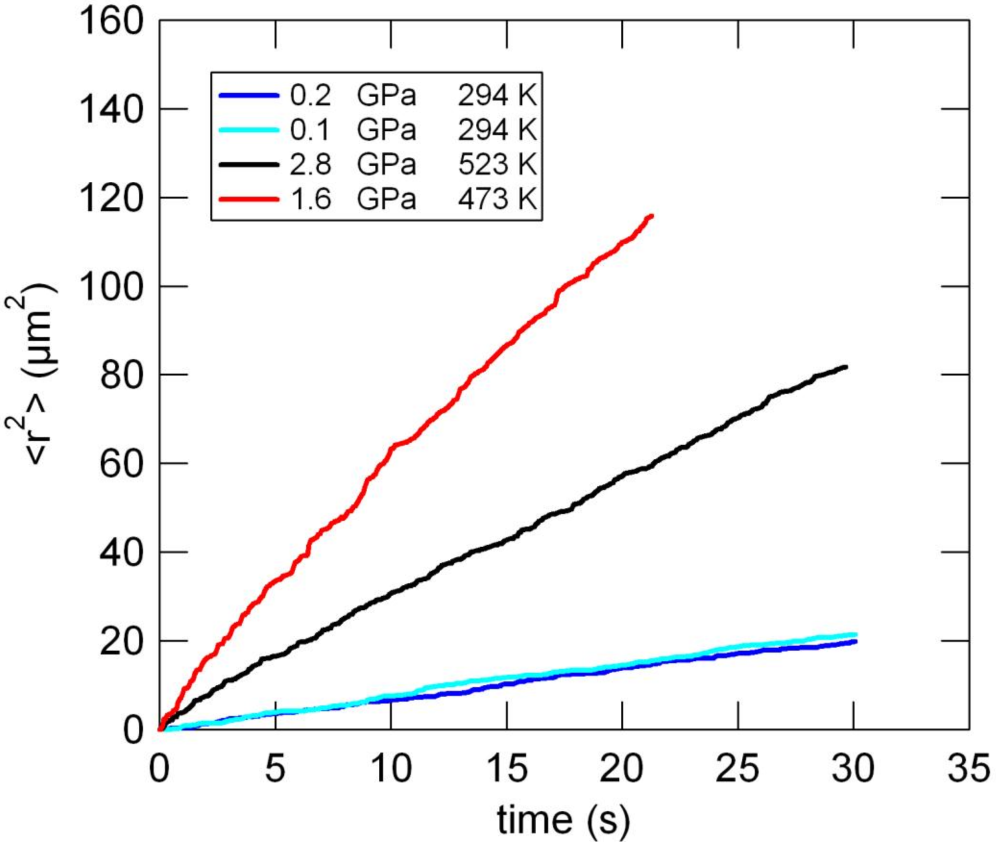

Figure 12: MSD as a function of time for the range of conditions covered in this study. The <r^2> values are averages of single particle MSDs.

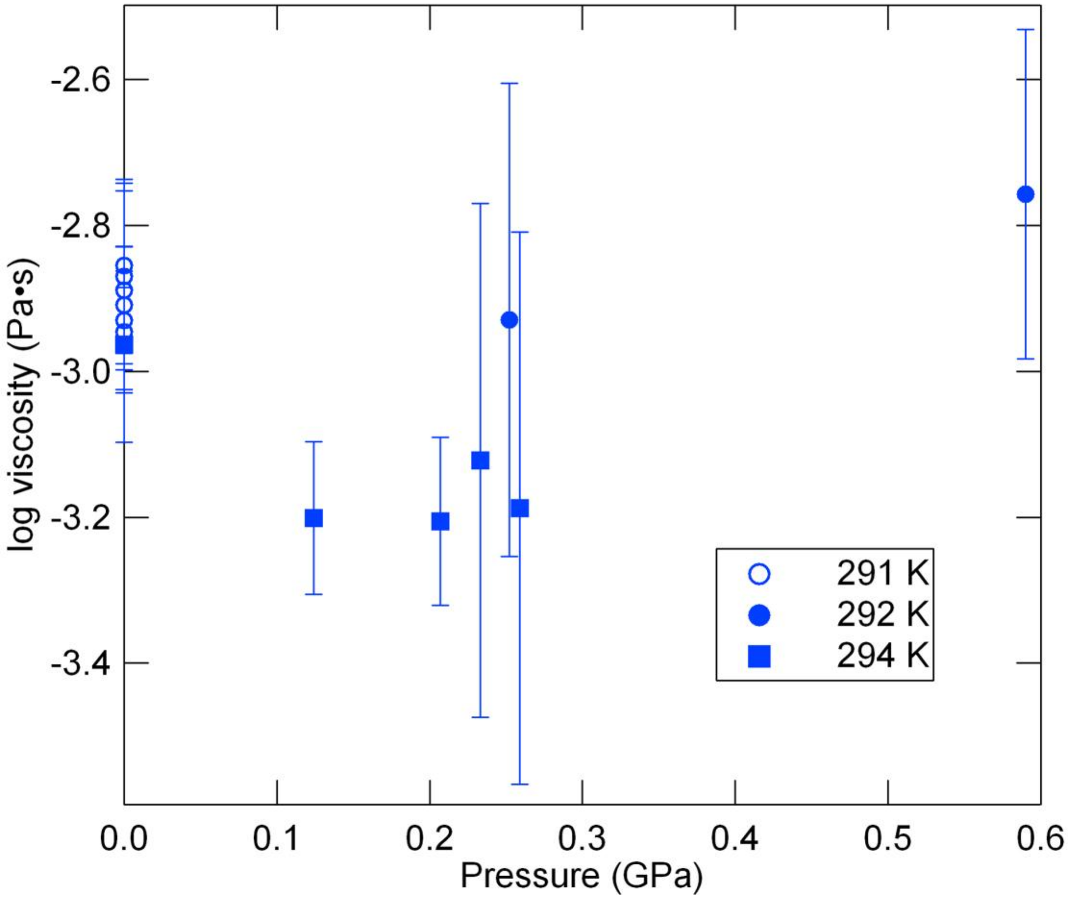

Figure 13: Viscosity as a function of pressure of experimental data from this study. The viscosity values represent the average value of the single particle viscosities weighted according to the uncertainties in the slopes. The error bars represent 1 standard deviation.

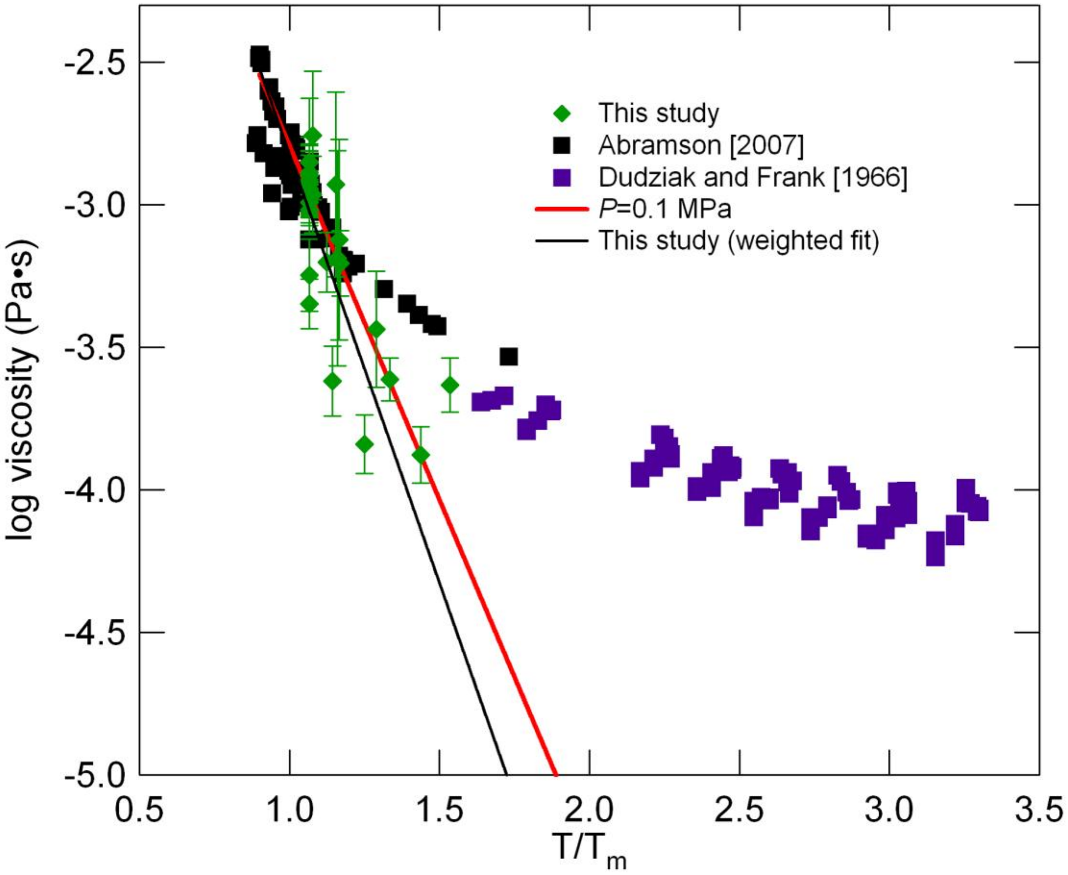

Figure 14: Viscosity data plotted as a function of homologous temperature. Black squares are data from *Abramson* [*2007*], purple squares are from *Dudziak and Frank* [*1966*], and green diamonds are data from this study. The red line is a fit to the 0.1 MPa data of *Aleksandrov and Trakhtengerts* [*1976*] and the black line is a weighted fit to the data from this study using Equation **(7)**. The high-pressure melting temperatures are based on the thermodynamic model by *Choukroun and Grasset* [*2007*] and the experimental data of *Lin et al* [*2004*].

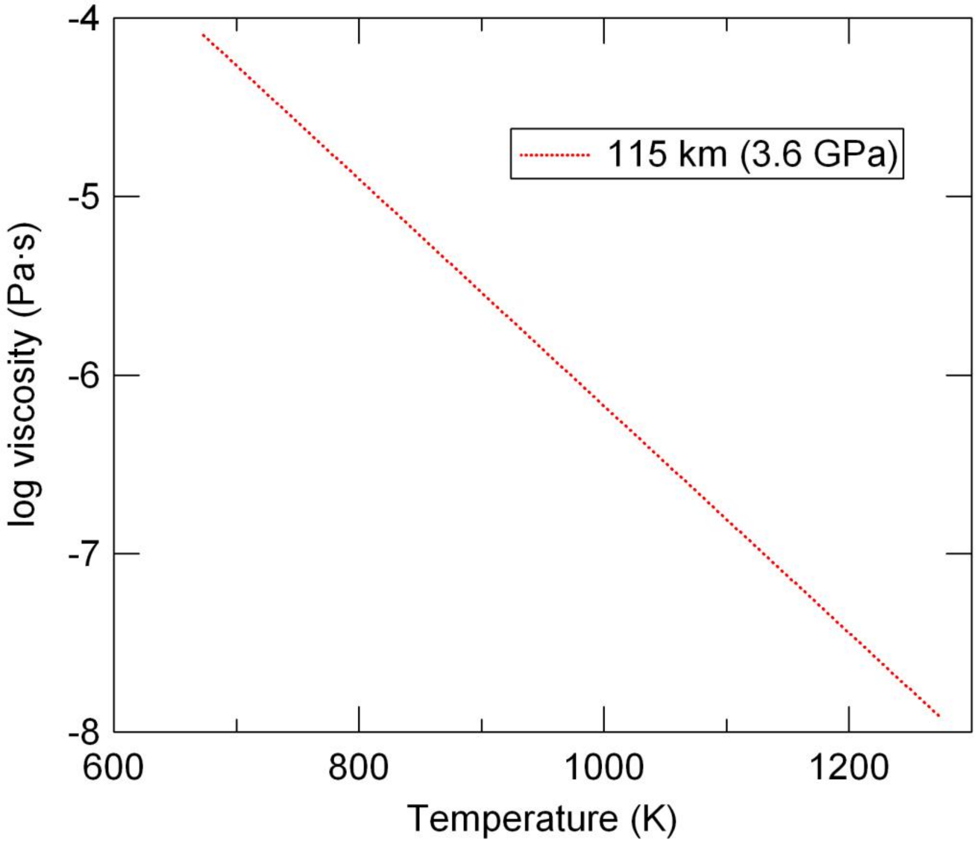

Figure 15: Viscosity of pure water at 115 km depth (3.6 GPa) as a function of temperature. The difference in viscosity of pure water as released from a cold slab and from a hot slab is a >6000 fold decrease. This difference is >1500% less than the effect of composition on water viscosity (*Keppler et al.*, 2004) such that the dominant factor in fluid viscosity at 115 km depth is composition.